

Sustainable production of AlSi10Mg parts by laser powder bed fusion process

Original

Sustainable production of AlSi10Mg parts by laser powder bed fusion process / Mercurio, Vincenza; Calignano, Flaviana; Iuliano, Luca. - In: INTERNATIONAL JOURNAL, ADVANCED MANUFACTURING TECHNOLOGY. - ISSN 0268-3768. - ELETTRONICO. - (2023). [10.1007/s00170-023-11004-0]

Availability:

This version is available at: 11583/2975388 since: 2023-01-30T15:39:39Z

Publisher:

Springer

Published

DOI:10.1007/s00170-023-11004-0

Terms of use:

This article is made available under terms and conditions as specified in the corresponding bibliographic description in the repository

Publisher copyright

Springer postprint/Author's Accepted Manuscript

This version of the article has been accepted for publication, after peer review (when applicable) and is subject to Springer Nature's AM terms of use, but is not the Version of Record and does not reflect post-acceptance improvements, or any corrections. The Version of Record is available online at: <http://dx.doi.org/10.1007/s00170-023-11004-0>

(Article begins on next page)

Sustainable production of AlSi10Mg parts by laser powder bed fusion process

Vincenza Mercurio, Flaviana Calignano*, Luca Iuliano

Politecnico di Torino, Department of Management and Production Engineering (DIGEP) - Integrated Additive Manufacturing Center (IAM) - Corso Duca Degli Abruzzi, 24 - 10129 Torino, Italy

*Correspondence: flaviana.calignano@polito.it; ORCID: 0000-0001-7672-7650

Abstract

Laser powder bed fusion (L-PBF) is an additive manufacturing technology that allows producing complex and lightweight parts without the use of specific tooling during the building process. However, despite continuous developments, some problems limit its use in series production. To introduce these systems in mass production, it is necessary to solve the problems and exceed the limits related to the requirements of industrialization: higher productivity, less material consumption, less over-production, and less waste, greater stability of the process, and higher quality of the final components. In this study, good practices to reduce resource consumption are presented. The production rate of the L-PBF technique was increased to produce AlSi10Mg alloy components. All the samples were manufactured with 90 μm layer thickness increasing productivity by approximately 65%. A design of experiments (DOE) method was used to analyze the effect of process parameters on the densification percentage. The produced samples were observed with a non-destructive process, the X-ray computed tomography system, to detect the presence of defects and pores. It has been found that a combination of parameters can induce porosities with a morphology such that after stress relieving the density increases rather than decreases as has been widely discussed in the literature. The mechanical properties are comparable with the literature values for conventional technologies. Good values of as-built surface roughness were also achieved despite the layer thickness.

Keywords: laser powder bed fusion; aluminum alloy; additive manufacturing; CT-scan; productivity; sustainability

1. Introduction

The laser powder bed fusion (L-PBF) process, also known as the selective laser melting (SLM) process, is one of the additive manufacturing (AM) techniques most used for near-net-shape components in the aerospace, robotics and automotive sectors [1–3]. The L-PBF process is a powder bed fusion technique that uses a laser beam as a heat source to selectively melt powder layer-by-layer [4, 5]. To date, two of the most important barriers to more widespread L-PBF in a small- and medium-sized companies (SME) environment are the high investment cost and the comparison with conventional technologies: cost of machines, re-design of components, raw materials, production, and post-processing [6]. Although the L-PBF technique allows producing complex metal parts with high accuracy and resolution due to finer layer thickness (typically 20 μm - 40 μm) and relatively small powder size distribution, layer-by-layer wise manufacturing is characterized by a slow build rate that further increases per-part cost and encourages applications in sectors where the production volumes are small and the high cost is not an important factor [7, 8].

To increase productivity and reduce building time, different solutions have been implemented by machine suppliers. The use of multiple laser beam sources allows for working on different areas simultaneously decreasing the exposure time [8–10]. The use of multi-lasers with different beam diameters is a recent method used to process particular samples which are required different levels of accuracy [10, 11]. It was proposed to use a laser beam with a higher power to melt more material. Double recoating, automated powder sieving systems, multi-powder hoppers, and bigger chamber volumes are other solutions implemented to reduce the manufacturing time. However, these modifications need increasingly expensive solutions leading to a higher total cost of machines, unsustainable for SMEs that could prefer to rely on an external supplier. Furthermore, many options have still issues that have to be overcome for mass production [8, 10, 12]. For this scope, a more practical strategy to increase productivity and reduce cost is needed, such as modifying process parameters and using particular measures during manufacturing which are the aims of this study.

2. Sustainability of the L-PBF process

In the literature, several studies face sustainability issues regarding the L-PBF process in terms of energy consumption [13, 14]. In this analysis, the entire process chain has been divided into three different phases and a distinction between time and cost was made among the sources of consumption (Fig. 1). In this way, a real perception of the resources implied in the process it is given to SMEs to better identify the critical points of the entire building process and methods to overcome them.

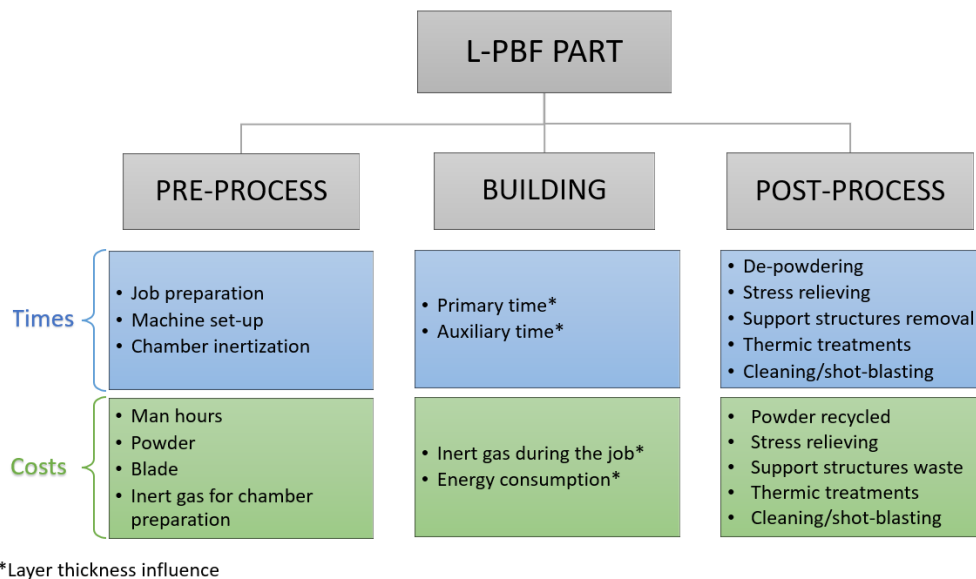


Fig. 1 The process chain of an L-PBF part with time and cost analysis

The phase of pre-processing is the first of the L-PBF process chain and data preparation, machine set-up, and chamber inertization are carried out. The data preparation begins with the exportation of a 3D CAD file in an STL format. Then, this file is repaired with suitable software and the manipulation of the file is carried out to optimize the orientation of the part and the support structures. The process parameters are assigned and therefore the slicing data (2D cross-sections) are obtained [15–18]. The machine set-up includes all actions by the operator to prepare the building process, such as pouring the un-melted powder into the dispenser, providing the recoating system with a suitable blade, pre-heating and aligning the building platform to allow a correct deposition of the powder

during the job. These two steps require variable time according to the complexity and height of the parts and the experience of the engineer and the operator. Finally, the inertization of the building chamber is required to avoid the oxidation and mechanical degradation of the components [14, 16]. The time needed for this step is fixed and not influenced by any factors. All these operations imply the consumption of resources that impacts on costing aspect: the man hours, the metal powder, the recoating blades, and the inert gas.

The powders used in the L-PBF process are usually produced by gas atomization to have a spherical shape and this involves high costs. The characteristics of the powders play a fundamental role in the quality of the final product. It has been shown that consistency and sphericity are important characteristics for having uniformity in the powder bed [19]. Although it is necessary to fill the entire build volume to the height of the tallest object to be produced, much of the dust is not directly exposed by the laser beam to produce the part itself. Therefore, reusing residual unfused powder allows companies to save money, reduce environmental impact, minimizing material waste. In addition, for industrial manufacturers, the ability to recover metal powders as many times as possible while maintaining compliance and manufacturing standards is a critical point. Although production is mainly conducted at room temperature in L-PBF, the powder can be degraded due to platform heating between 100 and 200 °C, oxidation of the powder (handling of the powder or during AM treatment in the chamber), and the formation of spatters during the process.

In many machines, there is the possibility to use two different recoater system types, hard or soft blades. Hard blades can be in high-speed steel (standard solution introduced by German company EOS GmbH) or in ceramic for magnetizable metals. Among the soft recoaters, there are carbon fiber brushes, and rubber or silicone blades. Many machine builders have introduced the soft blade due to the need to avoid interruptions during the process and thus complete the machining which is one of the main problems in using a steel blade. The hard blade assures a consistent layer thickness, high packing density to the powder bed, high precision, and less wear during construction. However, due to a non-optimal orientation of the workpiece, unsuitable process parameters, or failure of the supporting structures, the steel blade can jam leading to blocking of the machining or even violent detachment of the workpiece from the platform. This cannot happen with the soft blade because the blade tends to cut itself but not get stuck, completing the process. While it can help to complete a process that is not free from defects, on the other hand, it needs to be changed with each process thus creating waste material. Although the cost of a hard recoater is higher than it of a soft, the longer lifetime and the reduced needed maintenance make hard blades more cost-effective. The steel blades can be reused several times and reworked to restore the wire. However, this type of blade requires sensors on the recoating arm that can sense changes in force and stop over time before problems can arise. The insertion of these sensors is therefore an additional cost.

The building phase is the main process in which layer-by-layer the laser selectively melts the metal powder on a substrate plate. It is clear that the time consumed for the building is divided into primary and auxiliary times: the former is the actual exposure time and the latter is the time required for the movement of the axes, such as the lowering of the platforms and the deposition of the powder [20]. Both times depend on the process parameters. The costs are related to the consumption of inert gas that allows for maintaining a controlled-oxygen atmosphere for the entire building process and the actual energy consumption of the machine. Therefore, these costs vary according to the process parameters.

The post-process includes all operations allow to obtain end-use components: cleaning and removing the building platform from the working chamber, heat treatment due to internally-induced thermal stresses, removing of support structures, secondary thermic treatments, and shot-blasting to smooth the surface and preparing components for additional surface machining [14, 15, 17]. The particular structural characteristics that can derive from an alloy processed using L-PBF influence its machinability and surface quality [21]. All these operations can lead to an increase in time and cost for companies, so it is worth adopting correct measures to try to enhance the economic sustainability of the process.

3. Optimization of the process parameters

Due to the complexity of the laser powder bed melting process, the manufacturers of the L-PBF machines have developed sets of optimized processing conditions for each material. These include both machine settings which are generally not changed and process parameters which can be changed. There are over 200 processing parameters, among which the most commonly considered at the research level include laser power, layer thickness, laser scan speed, the distance between successive laser passes (also known as hatching distance), and scanning strategies (laser scanning pattern on each layer). The L-PBF exposure strategy is shown in Fig. 2. Generally, the hatch-contour (Fig. 2b₄ and 2c) exposure strategy is used in which the contour parameters are optimized for quality and precision, and the core (hatch or in-skin) parameters are optimized for density. The core parameters assume different values if this represents the down-skin or up-skin layer: in the first case they are optimized to make the part adhere to the supports or build platform, while in the second to improve the roughness. However, depending on the geometry, in some areas, these parameters can overlap (Fig. 2a).

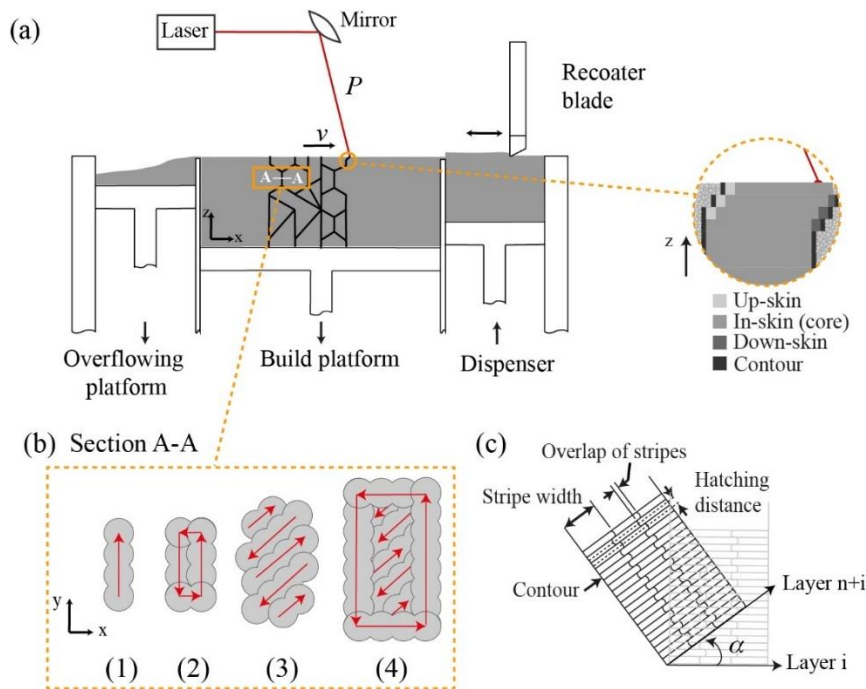


Fig. 2 Schematic depiction of the (a) L-PBF process and (b) exposure strategies of section A-A: (1) single track, (2) contour exposure, (3) hatch exposure, and (4) hatch-contour exposure. (c) Exposure strategy: α is hatch angle rotation

Optimized parameters are empirically derived to generally produce dense materials, minimize defects, reduce surface roughness, increase build rate, and produce parts with acceptable material properties. Due to the freedom of design of AM technologies and the diffusion of software systems for a generative design that allows for high geometric variations for the design of a component, it is not possible to have a set of parameters that will be fully optimized for all the characteristics of the parts (thin walls, thick sections, overhangs or others), material performance and process productivity. As a result, general parameter sets are developed to meet identified priorities and build possible geometries. Therefore, to identify the optimal parameters, one of the metrics commonly used is energy density. This is calculated based on a linear, areal, or volumetric approach with the volumetric being the most commonly used in the literature. The volumetric energy density (E_d) is defined by the laser power (P), scan speed (v), hatching distance (h_d), and layer thickness (t) as described in Eq.(1):

$$E_d = \frac{P}{t \cdot v \cdot h_d} \quad [\text{J/mm}^3] \quad (1)$$

The building rate is usually defined by the divisor factor in Eq. (1) [22, 23] and the main focus of this research is to achieve high build speeds by increasing the layer thickness. From Fig. 1 it is evident that increasing the layer thickness leads to a reduction of both times primary and auxiliary: due to fewer 2D cross-sections to be carried out the exposure time, recoating, and lowering platforms times decrease. The entire building time decreases. Consequently, the amount of inert gas to keep the oxygen level under a specific value and the energy consumption of the machine is reduced.

A case study on productivity optimization for the AlSi10Mg alloy is presented. The processing of aluminum alloys with L-PBF systems suffers from problems related to high reflectivity and thermal conductivity, and a strong tendency to oxidation [24]. The aluminum alloys that have shown major processability are the Al–Si–Mg cast alloys, especially AlSi10Mg followed by AlSi12 [20]. For AlSi10Mg alloy, layer thickness values from 40 μm to 100 μm were studied by analyzing various effects on the parts produced. Wang et al. [25] have explored the formation mechanisms and characteristics of porosity in AlSi10Mg components produced with a layer thickness of 40 μm and 80 μm . The lowest amount of pores was achieved with a layer thickness of 40 μm . Parveen et al. [26] investigate two different layer thicknesses such as 30 μm and 60 μm to evaluate layer thickness effects on microstructure and mechanical properties of the AlSi10Mg alloy samples produced by L-PBF. While the specimens exhibited similar tensile strength highlighting the possibility of increasing the layer thickness, the tensile properties of the 30 μm layer thickness samples were found to be better than the 60 μm layer thickness samples, plausibly due to low porosity, extremely fine microstructure, and improved surface morphology. Zavala-Arredondo et al. [22] have studied the densification mechanisms of high power (1 kW) L-PBF systems of AlSi10Mg alloy changing the process parameters. Characteristics of samples produced with a range of laser energy sufficient to process a layer thickness of 100 μm showed that thicker layers of AlSi10Mg alloy may require less laser energy than expected due to the typical properties of aluminum [22]. Depending on the thickness of the aluminum layer used in the L-PBF process, different oxygen contents can develop during the construction phase. Dadbakhsh and Hao [27] observed that a layer thickness of less than 50 μm in the aluminum alloy can develop higher amounts of oxide content than a layer of 75 μm . Thicker layers reduce oxygen by increasing the temperature and stirring within the melt pool. Therefore, lower laser energy may be required in the thicker layers as these reduce cooling rates, increase exothermic reaction and produce larger melt pools [27]. Layer thickness is therefore a fundamental parameter

that defines energy input requirements. Starting from the information obtained from the literature, in this study to achieve the set goal, laser power, and layer thickness were kept fixed to 370 W and 90 μm , while scanning speed and hatching distance were changed to obtain an optimal combination of parameters. To detect the quality obtained in terms of internal defects of the samples, X-ray 3D computed tomography (CT) was used. This technique is one of the non-destructive methods which allows to carry out of the aforementioned analysis [28, 29]: the samples aren't polished or grinded and so time and manual operations are saved [30].

4. Material and Methods

4.1 Material and equipment

A gas-atomized AlSi10Mg powder was used to produce the samples. The chemical composition of the powder (Table 1) complied with standard EN AC – 43000.

Elements	Al	Si	Fe	Cu	Mn	Mg	Ni	Zn	Pb	Sn	Ti
Wt. %	balance	9.0-11.0	<0.55	<0.05	<0.45	0.25-0.45	<0.05	<0.10	<0.05	<0.05	<0.15

Table 1 Chemical composition of AlSi10Mg powders.

The degradation of the powder makes reusability a challenging aspect particularly for AlSi10Mg as Al and Mg are highly reactive elements [31]. The powder exhibits some degree of variation in particle size and morphology after reuse. Generally, there is an increase in powder due to agglomeration which leads to an increase in the average size of particles and the number of satellites. At the same time, the number of fine (dimensionally smaller) particles decreases during continuous reuse, thus leading to a tighter particle size distribution. L-PBF requires particles in a narrow size range of 15–80 μm . Particles smaller than the lower limit typically show poor flowability when distributed by the blade over a previously deposited layer. On the other hand, particles with dimensions greater than the layer thickness (typically between 60 μm and 100 μm for a layer thickness of 30 μm and 50 μm respectively) are undesirable as they interfere with the powder diffusion process. Cordova et al. [32] showed that the material with the greatest variability concerning the particle size distribution, morphology, chemical composition, and flowability between Inconel 718, Ti6Al4V, AlSi10Mg, and Scalmalloy was AlSi10Mg after six reuse cycles. Maamoun et al. [33] studied the effect of reusing AlSi10Mg in 18 build cycles. The reused powder did not show apparent differences in the properties in comparison with the virgin powder. The morphology of reused particles was, however, slightly more elongated. A statistical study by Del Re et al. [34] of reusing AlSi10Mg throughout 8 build cycles revealed a systematic decrease of 10 MPa in the yield strength and UTS and a decrease from 160 to 145 MPa in the high cycle fatigue after eight cycles of reuse. However, reuse did not change the elongation at break and the surface quality of the produced specimens. The AlSi10Mg powder in this study was recovered for 8 cycles using an 83 μm mesh sieve without compromising mechanical properties and surface roughness (Figure 3). At each sieving, on 10 kg of powder, there was less than 1% waste due to the effects of spattering.

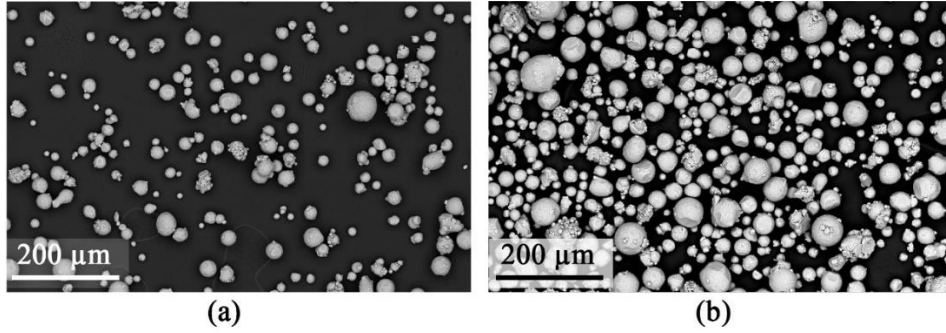


Fig. 3 SEM image of the (a) new and (b) recycled powder

Samples were produced by Print Sharp M250 laser powder bed fusion system. The machine is equipped with a 500 W Yb fibre laser with a focus diameter of 70-100 μm . The processing chamber was flooded with argon using a flow rate of 7 l/min and a gas flow speed of 1.43 m/s to hold the oxygen content below 0.1% during the complete processing time. To reduce residual stress and anisotropy a rotating stripes scan strategy with a rotation angle of 67° in each layer is used for the developed parameter set. To improve the thermal conductivity and the melting of the powder layer, the pre-heating temperature of the build platform was increased up to 100 $^\circ\text{C}$. The recoating systems tested in this work included a metal blade made of SS316L and a silicon blade. The machine has been designed to use only the silicone blade. It was therefore necessary to design a special steel blade to be inserted into the blade holder. Thanks to the blade design, mechanical vibrations are improved. During the experiments, it was noticed that without the necessary changes to the shape of the blade compared to the silicone one, the blade did not remain stable due to the vibrations due to the mechanical movement and how the recoater arm is designed which leaves a slight movement to the blade, generating surface ripples in the regions of the powder layer.

Norblast SD9 shot peening machine was used with glass microspheres at 6 bar in order to analyze the effect on the surface of the samples with and without re-melting.

4.2 Design of experiments and sample processing

Full factorial design of experiments (DOE) was used for 2 factors, scanning speed and hatching distance, with four levels to determine the relationship between factors affecting a process and the output of that process (Table 2).

A total of 48 cubic samples of 15 mm side were manufactured. After removing the build platform from the process chamber, the samples were cut from the build platform along the direction parallel to the xy-plane. An ultrasonic bath was used to remove the incompletely fused particles.

The same process parameters were used for the down-, in-, and up-skin in order to evaluate not only the density but also the surface roughness that these combinations of parameters generate. In this way, it is possible to define both the optimal parameters for density and also those for roughness. Two cases were considered for the up-skin: with (named case 1) and without (named case 2) re-melting. From various studies conducted [35–37], it has emerged that re-melting can significantly reduce surface roughness and defects. For the contour, the process parameters were selected considering linear energy ($E_L = P/v \cdot t$ [J/mm]). This value must be similar to that of the energy inside the core (down-, in-, or up-skin) in order to avoid melting problems in the overlapping areas.

	<i>Variable parameters</i>	<i>Fixed parameters</i>	<i>Value</i>
		Layer thickness [μm]	90
		Platform temperature [$^{\circ}\text{C}$]	100
		Laser beam [μm]	100
		Laser power [W]	370
		Scanning strategy	Stripes, rotated by 67°
Down-, in- and up-skin	Scanning speed [mm/s]		800, 900, 1300, 1400
	Hatching distance [mm]		0.09, 0.11, 0.12, 0.13
Contour	Laser power [W]		290, 340
	Scanning speed [mm/s]		700, 750, 1200, 1300
Build rate [mm^3/s]			6.48 - 16.38

Table 2 DOE parameters definition. Number of replications: 3

4.3 Cubic samples characterization

The relative densities of the samples were measured by Archimedes' principle with an analytical balance, KERN ABJ 320-4NM, accurate to ± 0.1 mg. Each cubic sample was measured three times and then an average value of measurements was calculated. All measurements were carried out in the air and distilled water and the influence of the temperature on fluid density was taken into account. Based on Archimedes' test results, some samples were selected to be analyzed by a CT machine (GE Phoenix v|tome|x s). The process parameters used for the scans were a voltage of 220 kV, a current of 160 μA , and a voxel size of 26.014 μm . The analyses were performed using the VGStudio Max 3.4 software. The software integrates specifications according to the BDG Reference Sheet P203 for the porosity analysis in slice images. The L-PBF process, depending on the process parameters and the quality of the raw powder, provides a specific porosity in the part. It is almost impossible to produce parts without internal pores. Spierings et al. [38] compared three techniques for detecting the density of metal components produced using L-PBF technology: Archimedes' method, microscopic analysis, and X-ray scanning. Based on these investigations, Archimedes' method allows for measuring the density of a piece in an easy, fast, and economical way. However, this method does not allow to have an idea about the three-dimensional arrangement of the internal pores. This is possible to obtain it in a non-destructive way only through CT. For this reason, wanting to analyze the effect of stress-relieving on the shape and size of the pores, an analysis of the samples with higher density was carried out both before and after the stress-relieving (SR). The high thermal gradients that occur during the manufacturing process also induce the accumulation of high residual stresses. To reduce these stresses before removing the component from the build platform, an SR treatment at 300 $^{\circ}\text{C}$ for 2 hours is commonly performed.

The surface roughness on the top surface and contour of as-built samples was measured with the use of RTP80 roughness tester by SM Metrology Systems to obtain the values of roughness average, R_a , and the average maximum height of the profile, R_z . The measurement distance was 4.8 mm and a 0.8 mm cut-off filter was used. The parameters chosen have been shown in the literature [39, 40] to be optimal for representing the surface of the L-PBF process. On each surface, three measurements were taken and the arithmetic mean of the measurements was used. A stereomicroscope, LEICA S9i equipped with an integrated 10 MP camera, was used to analyse the surface topography.

4.4 Tensile test

The tensile specimens and the test method were designed according to EN ISO 6892-1:2019 [41] (Fig. 4a). Uniaxial tensile tests were carried out, using an extensometer, with the 3MZ TENSILE model (EASYDUR) universal testing machine using a 10 tonnes load cell at a strain rate of 0.9 mm/min. Nine tensile specimens were manufactured in different positions on the build platform (Fig. 4b) with the combinations of scanning speed and hatching distance which have shown the best trade-off between the density and the build rate. The samples were divided into zones in order to verify the reproducibility of the data regardless of the position of the specimens on the platform. This, therefore, allows for verifying the goodness of the machine system for production purposes. A further reduction of the construction area, and therefore of the volume, would imply an effect on the production time. The tensile specimens were constructed only along the z -axis as it represents the worst condition [42, 43].

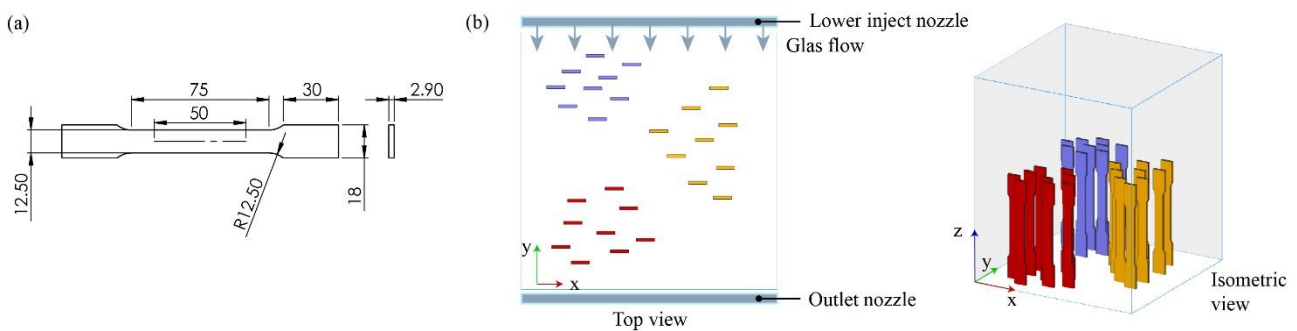


Fig. 4 (a) Geometrical dimension of the tensile specimens; (b) position of the specimens on the build platform: zone 1 (violet), zone 2 (yellow), and zone 3 (red)

5. Results and discussion

5.1 Density

The tested combinations of process parameters have led to values of energy density ranging from 22.59 J/mm³ to 57.10 J/mm³. Looking at Fig. 5, it is possible to notice an increase in density with increasing scanning speed and hatching distance (Fig. 5a) in correspondence with an increase in build rate and decrease in energy density (Fig. 5b).

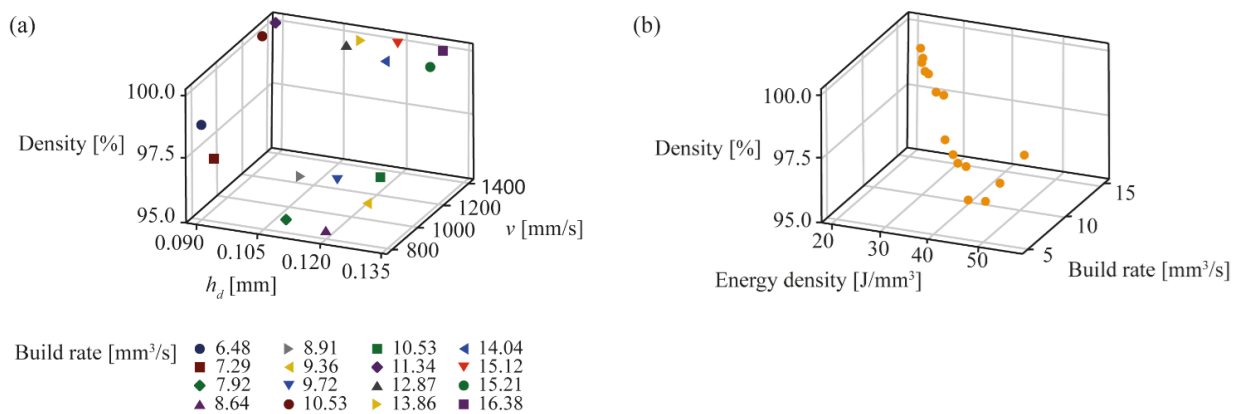


Fig. 5 Three-dimensional scatterplot of density: (a) density vs scanning speed and hatching distance; (b) density vs build rate and energy density

Furthermore, it is possible to see the presence of two identical production values ($10.53 \text{ mm}^3/\text{s}$) which, however, correspond to different density values. Various studies have highlighted the limits of the energy density and how its simplified formula is not able to uniquely identify a result and therefore a window of realistic process parameters [4, 20, 44–46]. This can also be extended to the formula used for productivity calculation. Since the build rate is the denominator of the energy density, it is clear to understand how as the first increases, the second decreases. There is therefore such a limit that it is not possible to increase productivity too much without compromising the characteristics of the components produced [47].

Analyzing the effects of the two parameters through the analysis of variance (ANOVA), it appears, as known in the literature [48, 49], that both parameters have a high effect on density (Table 3).

Source	DF	Adj SS	Adj MS	F-value	p-value
Model	15	75.3596	5.0240	174.90	0.000
Linear	6	65.0729	10.8455	377.56	0.000
v	3	61.3605	20.4535	712.04	0.000
h_d	3	3.7124	1.2375	43.08	0.000
2-Way Interactions	9	10.2868	1.1430	39.79	0.000
$v*h_d$	9	10.2868	1.1430	39.79	0.000
Error	32	0.9192	0.0287		
Total	47	76.2788			

Table 3 ANOVA of the density. $R^2=98.79\%$, $R^2(\text{adj})=98.23\%$

However, what emerges from the plots in Fig. 6 is that scanning speed has a more pronounced effect than the hatching distance. The interaction analysis shows that regardless of the hatching distance value, increasing the scanning speed from 900 mm/s to 1300 mm/s allows for a rapid increase in density. After this scanning speed value, the density does not tend to increase. Samples with high density and related parameters are shown in Table 4.

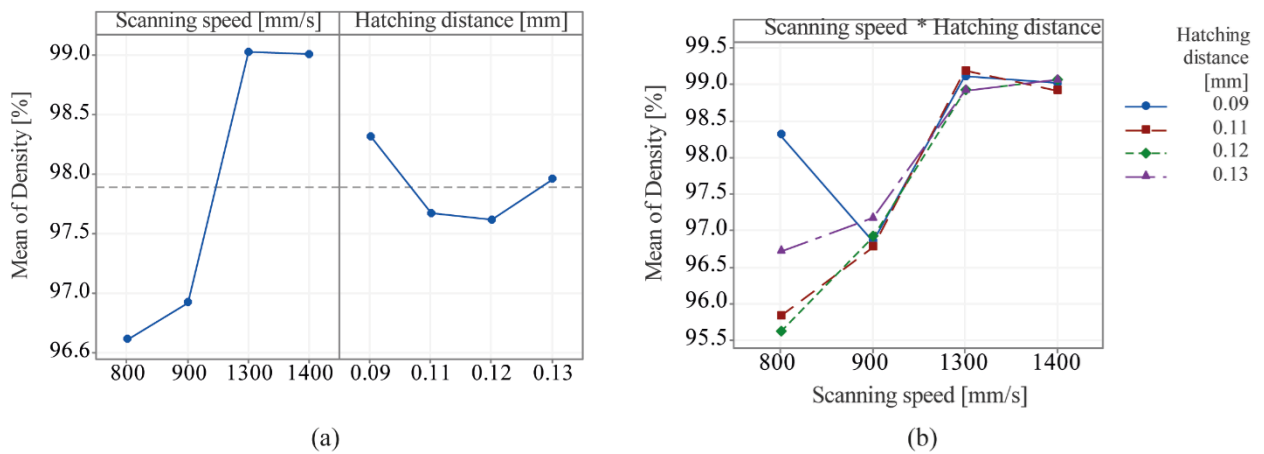


Fig. 6 Plots of the (a) main effects and (b) of the interaction for density

Number sample	Scannin speed [mm/s]	Hatching distance [mm]	Build rate [mm ³ /s]	Density [%] with Std
S1	1400	0.13	16.38	99.06 ± 0.19
S10	1400	0.09	11.34	99.02 ± 0.12
S12	1400	0.12	15.12	99.06 ± 0.14
S13	1300	0.09	10.53	99.11 ± 0.08
S15	1300	0.11	12.87	99.19 ± 0.03

Table 4 Samples with the highest density

In order to analyze the results obtained by Archimedes' method and understand the differences between the samples with higher density and productivity, samples S1, S12 and S15 were analyzed with the CT. Sample S15, despite having lower productivity than the other two, was analyzed to understand the difference in terms of defects with the others. Fig. 7 shows the CT images of samples before and after SR and the size pore percentage.

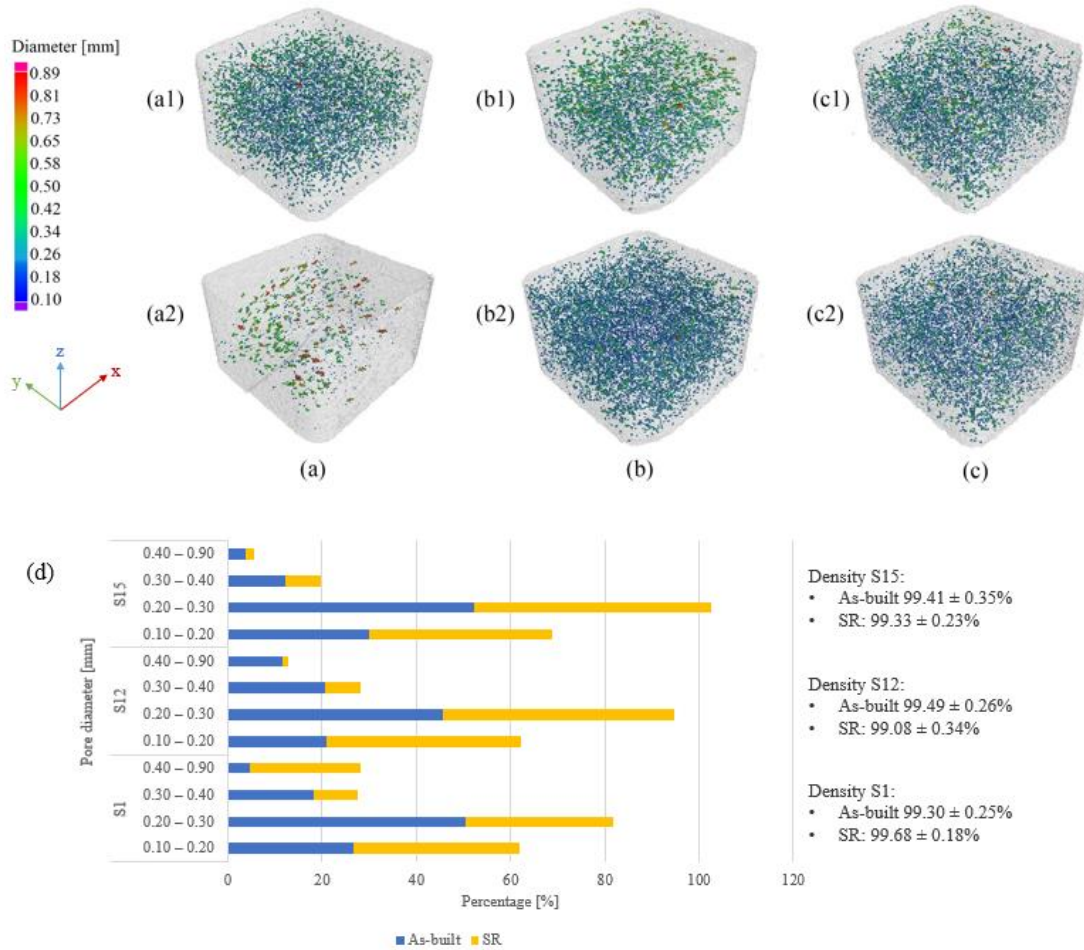


Fig. 7 CT-scan images: (a) S1, (b) S12, and (c) S15. (a1), (b1), and (c1) as-built; (a2), (b2), and (c2) after SR. (d) Density and size of porosity by CT analysis

Observing Fig. 7 it is possible to notice a different size of the pores before and after the SR. In particular, while for sample S1 there is a considerable reduction of the porosity in samples S12 and S15 the porosity increases by reducing the density. A similar result was found by Babamiri et al. [50] with Inconel 718 where the total void volume ratio decreased by 29.7% from as-built to SR. The void

volume ratio, which represents the total volume of porosity divided by the total volume of X-rays, has therefore decreased by similar percentages due to SR. Observing the process parameters between sample S1 and S12 the difference lies in a 0.01 mm in the hatching. This difference, although minimal at the numerical level, is not such in the process and can induce slightly different defects which, after the SR, which releases the trapped gas and modifies the microstructure as widely highlighted in the literature, acts on the morphology of the pores with small diameters. To explain the observed porosity reduction, the authors assumed that the SR process helps correct common defects in layer additive manufacturing, such as trapped gas bubbles in the melt pool and lack of fusion (LOF) caused by the beam not completely dissolving the powder. What is noticeable in this study is a different distribution of the pore sizes between as-built and SR. In parts manufactured using L-PBF technology, two main types of pores can be generated [48, 51]. The first type has a spherical morphology with dimensions up to tens of microns and these are generally classified as metallurgical pores. The second type of pore has an irregular morphology and is approximately hundreds of microns larger in size. Generally, this type of porosity extends over several levels. Therefore, in order to better understand the effect of SR on density and therefore on porosity by identifying the shape of the pores and therefore the type, an analysis of sphericity [52] was carried out through the images obtained by CT-scan [53]. Sphericity (Ψ) indicates the shape of a pore and is defined as the ratio of the surface area of a sphere having the same volume as the pore to the pore's surface area [52]:

$$\Psi = \frac{\pi^{\frac{1}{3}}(6V_p)^{\frac{2}{3}}}{A_p} \quad (2)$$

where V_p is the pore volume and A_p is the pore's surface area. The more this value is equal to 1, the more the pores have a shape corresponding to a sphere. Fig. 8 shows the number of pores with respect to pore diameter and an indication of the sphericity of these pores. Pores with $\Psi > 0.6$ are indicative of residual gases in the powder or gas that become trapped due to the turbulence of the melt flow generated by excessive laser energy or high scanning speeds. These are generally isolated within solidified melt pools. The high energy can also cause localized vaporization which leads to the formation of keyhole pores - spherical pores deep in solidified pools. This defect can manifest as larger or irregular spherical shapes ($\Psi < 0.6$) with keyhole instability (rapid solidification with an incomplete filling of the gaps). Irregular pores are generally attributed in Al alloys to two causes: (i) LOF between adjacent layers or partially fused powder particles when insufficient energy is applied; (ii) failure to effectively destroy the oxide films present in the powder. The defects of the oxide film can be introduced both by overheating with high energy, and by the instability of the melt pool caused for example by the Marangoni force and the recoil pressure [54] that occurs at high scanning speeds. Although sphericity combined with pore size can be used to distinguish between gas-like pores and other specific defect mechanisms, it cannot be used to adequately quantify the three-dimensional pore shape of highly irregular elements. For example, pores showing low sphericity can be relatively equidimensional or, conversely, stretched along one or two axes in the Cartesian plane. Different physical forms of pores can affect macroscopic mechanical properties as well as their location (internal or near-surface pores) [55]. For this reason, starting from the sphericity values, the dimension of the bounding box surrounding the defect in the scene coordinate system is considered. In this way the shape of the ellipsoid within which the pore is enclosed is defined to understand if it expands preferably along the layer (dimension on the xy -plane > than that on the xz - and yz -planes) or between the layers (dimension on the xy -plane < than that the one on the xz - and yz -planes) as it determines how much that pore can affect the mechanical properties.

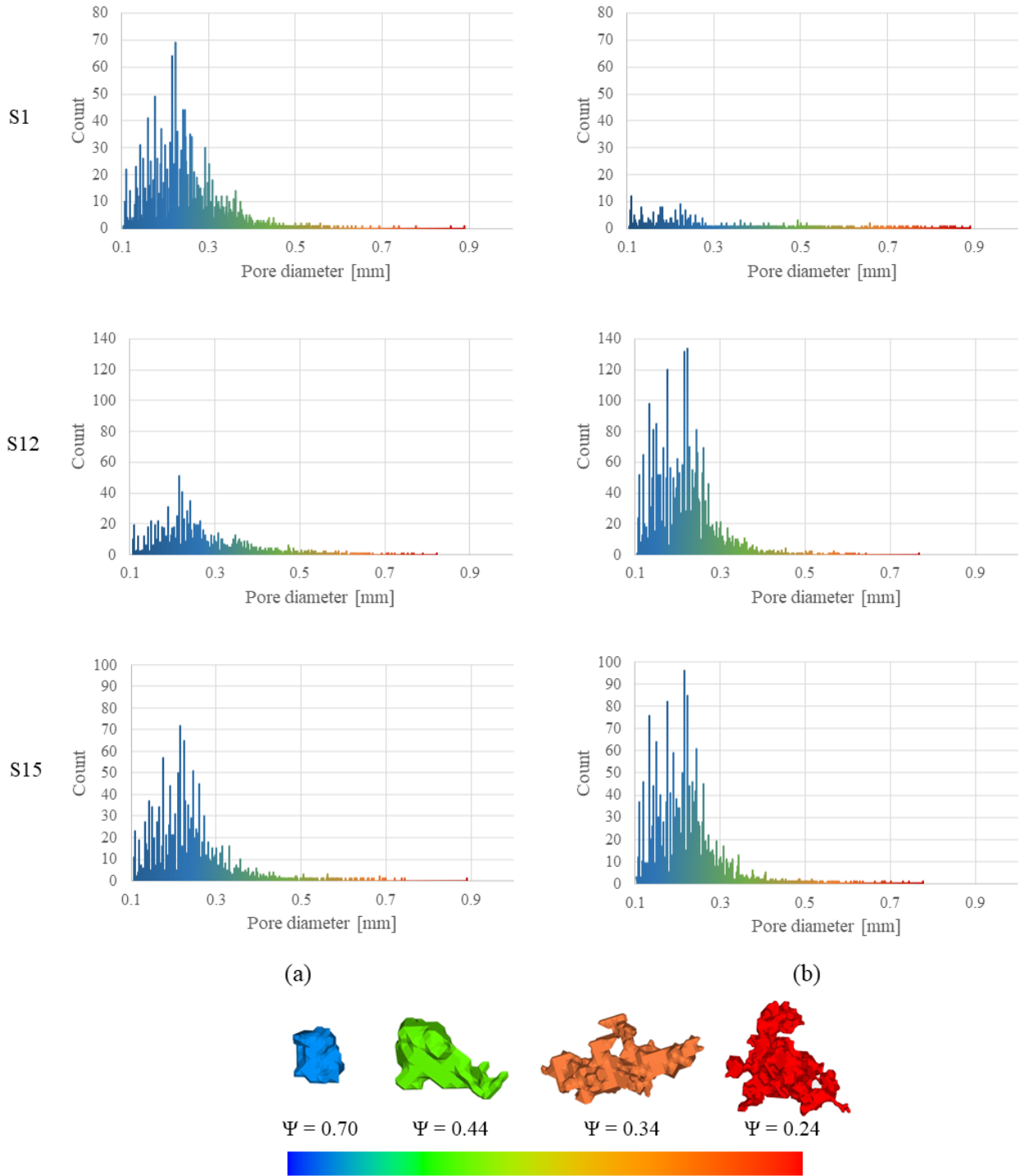


Fig. 8 Pore diameter (a) as-built and (b) after SR. The colour map indicates the sphericity

Shape analysis denotes that the principal directions are the x - and y - directions with respect to the construction z -axis (Fig. 9). These defects with a larger area perpendicular to the construction direction are typically classified as LOF. If the greater area were oriented parallel to the construction direction, shrinkage porosity (generated during the solidification phase) could be created which could result in the propagation of a crack in the fatigue life of a component.

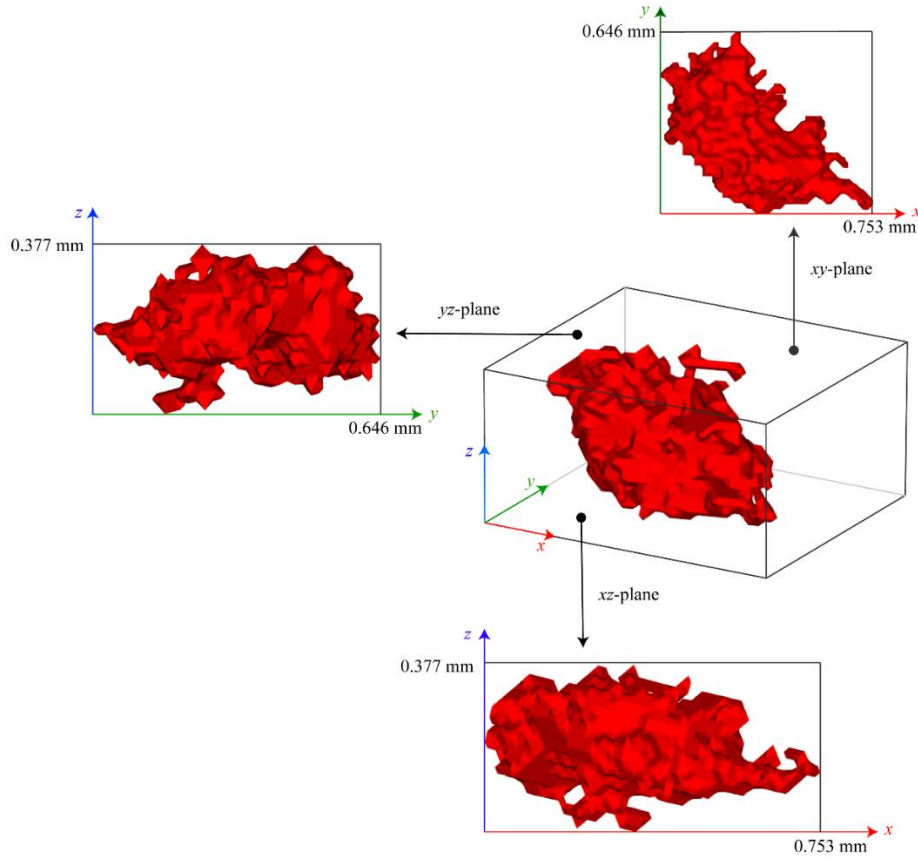


Fig. 9 Bounding box of the pore with $\Psi=0.34$ in the S1 sample

From the analysis of a layer (Fig. 10), it is observed that some particles are sintered on the stripes and these residual particles are typical splatters of solidified liquid. The size of the spatter can be much larger than the size of the raw powders. When a few splatters of cold particles enter the laser beam region, the particles can be fused into small droplets. From the collision of these small droplets, large splatters can form which solidified can cause defects in the as-built part. These defects arise both because splatters may have a high oxygen content, which reduces substrate wetting [56], and because large splatters may not be fully fused during laser scanning, thus becoming potential pore generation sites [57]. The types of pores and the size of the layer suggest that a series of LOF pores have been generated around the splatters, which is clear evidence of the defects caused by the splatters. In fact, the size of the layer can increase or attenuate the powder splattering. The jet of steam typically has the shape of an inverted cone that is more confined near the molten pool but wears away as it moves away from the molten pool. Therefore, a powder bed with a thickness of 30 μm has a better chance of being completely dissolved by the laser and leaving fewer loose powders in the path of the vapor jet to be expelled than a 90 μm layer. A similar result was found by Zavala-Arredondo et al. [22]: analyzing the construction of AlSi10Mg samples with different layer sizes, the authors observed that a greater layer thickness limits the densification mechanism, possibly due to the development of deeper melts that promote keyhole porosity.

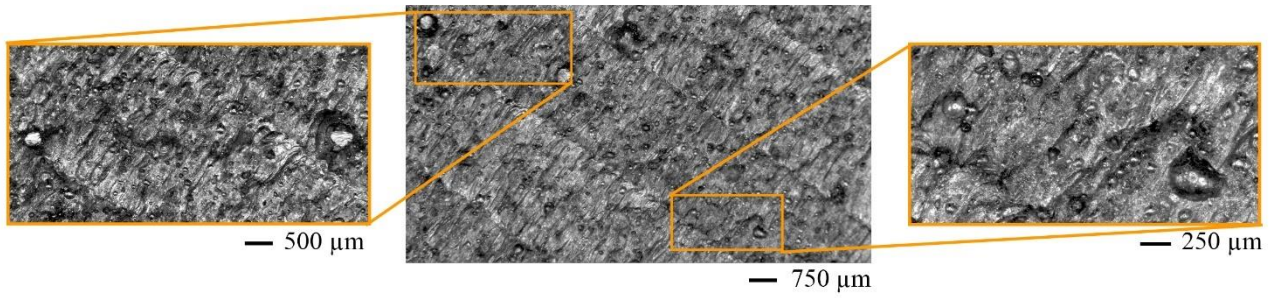


Fig. 10 Stereomicroscope images of spatter particles on the layer

Another factor to consider when looking at the samples (Fig. 10) is the generation of pores due to the passage of the blade. When the spattering particles are present on the surface, these are further removed with the recorder blade during the coverage of the layer causing the formation of pits and ridges on the surface which will therefore have different heights generating possible pores and, in the case of the last layers, greater surface roughness. The type of blade used can amplify the effect of the pores. A steel blade, in fact, hardly wears out and generates greater pressure during application on the layer of powder and therefore on the previously melted areas with consequent improvement or, if the parameters are not optimal or there are agglomerations in the powder, a deterioration of the surface. Depending on the material being processed, a silicon/rubber/carbon fibers blade may deteriorate quickly at some points, generating an uneven deposition layer and possible notches in contact with the previously melted area due to, for example, spattering particles. This, therefore, leads to areas more susceptible to the formation of pores.

5.2 Surface roughness

The surface roughness values in terms of R_a and R_z are very similar regardless of the parameters. In case 1 (with re-melting) the values obtained are $R_a = 4.14 \mu\text{m} \pm 0.70 \mu\text{m}$ and $R_z = 18.92 \mu\text{m} \pm 2.89 \mu\text{m}$, while, in case 2 (without re-melting), the values are $R_a = 14.56 \mu\text{m} \pm 3.60 \mu\text{m}$ and $R_z = 67.70 \mu\text{m} \pm 17.01 \mu\text{m}$. Analyzing the parameters individually, the values that allow the lowest roughness ($R_a = 2.37 \mu\text{m}$ and $R_z = 11.37 \mu\text{m}$) are: for the case 1 $v = 900 \text{ mm/s}$ and $h_d = 0.11 \text{ mm}$, for the case 2 $v = 1300 \text{ mm/s}$ and $h_d = 0.11 \text{ mm}$. Even considering the profile-induced roughness, there are few differences even if different parameters were used. In this case, the following roughness values were obtained: $R_a = 18.92 \mu\text{m} \pm 2.95 \mu\text{m}$ and $R_z = 94.46 \mu\text{m} \pm 3.20 \mu\text{m}$. From Fig. 11 it is possible to see the clear difference between the two cases. The re-melting takes place on an already melted surface and not on a layer of powder and this leads to a better melting of the layer, reducing defects (e.g. spatters) and highlighting the trace of the laser inside the stripe. By observing the contour, however, it is possible to note the absence of the stair-case effect that should be evident in cases with such high thicknesses. This highlights a good fusion of the levels.

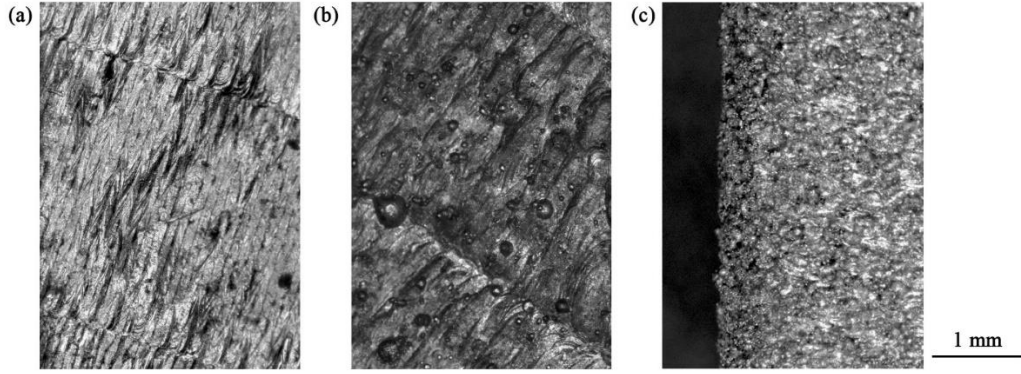


Fig. 11 Surface roughness of the up-skin: (a) with re-melting and (b) without re-melting. (c) Surface roughness of the contour

Fig. 12 shows the three-dimensional surfaces before and after shot peening. The surface in case 1 has become more uniform and traces are no longer visible but this has led to an increase in R_z by 26% and a reduction in R_a by 5%. In case 2, on the other hand, the reduction of R_a is 54% and for R_z of 52%. Also at the level of contour roughness, there was a roughness reduction of R_a by 35% and R_z by 40%. This high reduction in case 2 and the boundary is mainly due to the removal of the unfused particles. In case 1, on the other hand, the pressure of the jet and therefore of the bombardment of the glass microsphere on the surface may have induced an increase in ridges and valleys, and therefore of R_z due to the ductility of the aluminum.

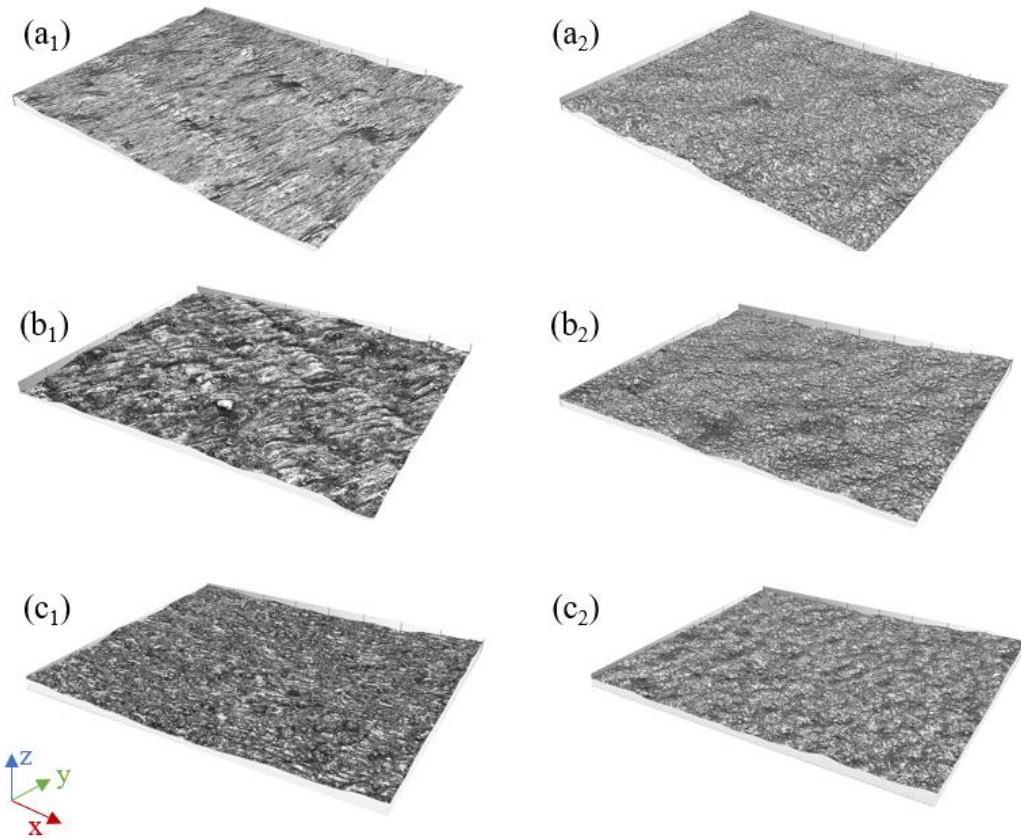


Fig. 12 Three-dimensional surface. Case 1 (a₁) as-built and (a₂) shot peened; case 2 (b₁) as-built and (b₂) shot peened; Contour (c₁) as-built and (c₂) shot peened

5.3 Tensile test

Table 5 shows the tensile results compared with reference values of mechanical performances of the same die-cast alloy. The mechanical properties of specimens are comparable with specimens produced by conventional techniques, as already noted in the literature [58–60]. Furthermore, the values are comparable with those obtained in the *xy*-direction, normally considered the best condition with respect to the *z*-direction, found by Anwar and Pham [61] produced with a layer thickness of 100 μm . A significant reduction in strength (yield and ultimate) is detected for stress-relieved samples as reported in the literature [62, 63]. Regarding the position of the samples on the construction platform, no high differences in mechanical properties were found between the samples placed in the different areas (Fig. 4b). However, the samples in zone 2 showed slightly higher values (approximately 2.6%) than in the other two zones. Studies in the literature [64, 65] have shown that according to the flow rate of the inert gas, samples placed in a position close to the gas inlet or far away can have more defects than samples placed in the central position of the build platform. Fig. 13 shows the CT image of the porosity of the tensile specimen, and relative density, in the zone of the break before the tensile test and the break after the test. As can be seen, in the failure area of the specimen there are no pores with diameters greater than 0.3 mm and they have a sphericity of 0.7 such as not to encourage the initiation of a crack.

	<i>Yield strength</i> [MPa]	<i>Ultimate tensile strength</i> [MPa]	<i>Elongation at break</i> [%]
S1 as-built_zone 1	178 \pm 6.36	298 \pm 0.71	2.5 \pm 0.07
S1 as-built_zone 2	189 \pm 6.36	306 \pm 4.24	2.5 \pm 0.14
S1 as-built_zone 3	170 \pm 7.78	282 \pm 0.71	2.1 \pm 0.14
S1 SR_zone 1	149 \pm 7.00	235 \pm 7.00	4.2 \pm 0.39
S1 SR_zone 2	151 \pm 4.74	241 \pm 8.45	4.2 \pm 0.15
S1 SR_zone 3	141 \pm 0.18	216 \pm 4.01	3.5 \pm 0.84
Conventional cast and Aged [66]	170	300-317	3.6
High pressure die casting F* [66, 67]		300-350	3-5
High pressure die casting T6* [66, 67]		330-365	3-5

Table 5 Tensile test results in *z*-direction. *For the high pressure die casting AlSi10Mg parts, the properties for as-cast (F) as well as for the aged (T6) condition are given

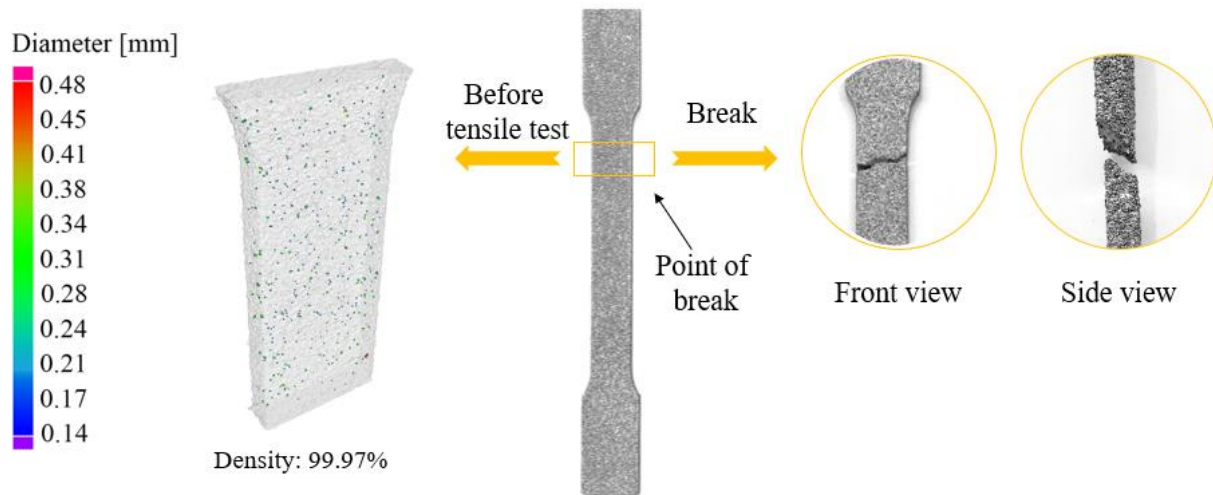


Fig. 13 Tensile specimen with CT image of porosity and the point of the break

Conclusion

This study analyzes a way to reduce production time and waste which has a consequence on the costs affecting the L-PBF process (gas, consumables, energy, etc). For example, correct recycling of the powders and a suitable recoating system could lead to a better production process with less waste generation. Furthermore, it was demonstrated that it is possible to increase the L-PBF productivity of AlSi10Mg considerably without modifying the machine with expensive solutions. The density, mechanical properties, and surface roughness were not compromising. Through the use of non-destructive tools such as tomography, it is possible to analyze the types of defects in more detail to understand how much they can affect mechanical characteristics. The main results achieved are summarized below:

- After the SR the sample constructed with parameters $P = 370\text{W}$, $v = 1400\text{ mm/s}$, and $h_d = 0.13\text{ mm}$ showed a density of 99.80% with few irregular pores;
- Considering the production times calculated using the L-PBF system software, the transition from a layer thickness of $30\text{ }\mu\text{m}$, normally used, to $90\text{ }\mu\text{m}$ led to a 65% reduction in production time;
- The analysis of the pore shape revealed defects with a larger area perpendicular to the construction direction which is generally classified as LOF;
- The porosity after SR can vary in terms of the number and size of the pores especially when these are mainly due to trapped gas;
- The defects mainly found are due to the effect of the spatter;
- The use of CT-scan has allowed to expand the analysis on the effects of process parameters and SR treatment on internal defects. The results obtained are a first example of a phenomenon not highlighted previously for the AlSi10Mg and this thanks to the use of non-destructive tools;
- By optimizing the process parameters of the contour concerning the parameters used for the in-skin, it is possible to obtain samples built with a $90\text{ }\mu\text{m}$ layer without the stair-case effect which leads to better accuracy;
- The as-built surface roughness is significantly reduced compared to the general values defined for this process if re-melting is used. However, it is possible by shot-peening to further reduce

the values and surface topography as long as the jet rate of the shot-peening is optimized so as not to compromise the surface due to the ductility of the aluminum;

- The mechanical properties of the samples constructed in the direction of build highlighted in the literature as being worse than that on the *xy*-plane are comparable with the samples produced with conventional techniques and with values found in the literature. As already highlighted in the literature, SR reduces mechanical properties even if it induces an improvement in porosity.

Acknowledgments

The authors would like to thank Giovanni Marchiandi and Matteo Perrone for their support of the depicted research into the suitable modifications to the used L-PBF system.

Statements and Declarations

a. Funding

The authors declare that no funds, grants, or other support were received during the preparation of this manuscript

b. Competing Interests

The authors have no relevant financial or non-financial interests to disclose.

c. Availability of data and material

Not applicable

d. Code availability

Not applicable

e. Ethics approval

Not applicable

f. Consent to participate

Not applicable

g. Consent for publication

Not applicable

h. Author Contributions

Vincenza Mercurio: Methodology, Formal analysis, Investigation, Validation, Writing - original draft preparation, Writing - review and editing. **Flaviana Calignano**: Supervision, Conceptualization, Methodology, Investigation, Validation, Formal analysis, Writing - original draft preparation, Writing - review and editing. **Luca Iuliano**: Supervision, Resources.

References

1. Sefene EM (2022) State-of-the-art of selective laser melting process: A comprehensive review. *J Manuf Syst* 63:250–274. <https://doi.org/10.1016/J.JMSY.2022.04.002>
2. Peverini OA, Addamo G, Tascone R, et al (2015) Enhanced topology of E-plane resonators for high-power satellite applications. *IEEE Trans Microw Theory Tech*. <https://doi.org/10.1109/TMTT.2015.2462839>
3. Semini C, Goldsmith J, Manfredi D, et al (2015) Additive manufacturing for agile legged robots with hydraulic actuation. In: *Proceedings of the 17th International Conference on Advanced Robotics, ICAR 2015*
4. Calignano F, Cattano G, Manfredi D (2018) Manufacturing of thin wall structures in

- AlSi10Mg alloy by laser powder bed fusion through process parameters. *J Mater Process Technol.* <https://doi.org/10.1016/j.jmatprotec.2018.01.029>
5. Pfaff A, Bierdel M, Hoschke K, et al (2020) Resource analysis model and validation for selective laser melting, constituting the potential of lightweight design for material efficiency. *Sustain Prod Consum.* <https://doi.org/10.1016/j.spc.2019.12.004>
6. Yi L, Gläßner C, Aurich JC (2019) How to integrate additive manufacturing technologies into manufacturing systems successfully: A perspective from the commercial vehicle industry. *J Manuf Syst* 53:195–211. <https://doi.org/10.1016/j.jmsy.2019.09.007>
7. Leicht A, Fischer M, Klement U, et al (2021) Increasing the Productivity of Laser Powder Bed Fusion for Stainless Steel 316L through Increased Layer Thickness. *J Mater Eng Perform* 30:575–584. <https://doi.org/10.1007/s11665-020-05334-3>
8. Schwerz C, Schulz F, Natesan E, Nyborg L (2022) Increasing productivity of laser powder bed fusion manufactured Hastelloy X through modification of process parameters. *J Manuf Process* 78:231–241. <https://doi.org/10.1016/j.jmapro.2022.04.013>
9. Paradise P, Patil D, Van Handel N, et al (2022) Improving Productivity in the Laser Powder Bed Fusion of Inconel 718 by Increasing Layer Thickness: Effects on Mechanical Behavior. *J Mater Eng Perform* 31:6205–6220. <https://doi.org/10.1007/s11665-022-06961-8>
10. Khorasani AM, Gibson I, Veetil JK, Ghasemi AH (2020) A review of technological improvements in laser-based powder bed fusion of metal printers. *Int J Adv Manuf Technol* 108:191–209. <https://doi.org/10.1007/s00170-020-05361-3>
11. Soylemez E (2020) High deposition rate approach of selective laser melting through defocused single bead experiments and thermal finite element analysis for Ti-6Al-4V. *Addit Manuf* 31:100984. <https://doi.org/10.1016/j.addma.2019.100984>
12. Schneck M, Schmitt M, Schlick G (2020) Supply Chain and Cost Evaluation for Laser Powder Bed Fusion. *Proc 2020 IEEE 10th Int Conf "Nanomaterials Appl Prop N 2020 9–13.* <https://doi.org/10.1109/NAP51477.2020.9309677>
13. Priarone PC, Lunetto V, Atzeni E, Salmi A (2018) Laser powder bed fusion (L-PBF) additive manufacturing: On the correlation between design choices and process sustainability. *Procedia CIRP* 78:85–90. <https://doi.org/10.1016/j.procir.2018.09.058>
14. Ochs D, Wehnert KK, Hartmann J, et al (2021) Sustainable Aspects of a Metal Printing Process Chain with Laser Powder Bed Fusion (LPBF). *Procedia CIRP* 98:613–618. <https://doi.org/10.1016/j.procir.2021.01.163>
15. Groneberg H, Horstkotte R, Pruemmer M, et al (2022) Concept for the reduction of non-value-adding operations in Laser Powder Bed Fusion (L-PBF). *Procedia CIRP* 107:344–349. <https://doi.org/10.1016/j.procir.2022.04.056>
16. Calignano F, Manfredi D, Ambrosio EP, et al (2017) Overview on additive manufacturing technologies. *Proc IEEE* 105:593–612. <https://doi.org/10.1109/JPROC.2016.2625098>
17. Dev Singh D, Mahender T, Raji Reddy A (2021) Powder bed fusion process: A brief review. *Mater Today Proc* 46:350–355. <https://doi.org/10.1016/j.matpr.2020.08.415>
18. Calignano F (2014) Design optimization of supports for overhanging structures in aluminum and titanium alloys by selective laser melting. *Mater Des.* <https://doi.org/10.1016/j.matdes.2014.07.043>
19. Mussatto A, Groarke R, O'Neill A, et al (2021) Influences of powder morphology and spreading parameters on the powder bed topography uniformity in powder bed fusion metal additive manufacturing. *Addit Manuf.* <https://doi.org/10.1016/j.addma.2020.101807>
20. Aboulkhair NT, Simonelli M, Parry L, et al (2019) 3D printing of Aluminium alloys: Additive Manufacturing of Aluminium alloys using selective laser melting. *Prog Mater Sci* 106:100578. <https://doi.org/10.1016/j.pmatsci.2019.100578>
21. de Oliveira AR, Del Conte EG (2021) Concurrent improvement of surface roughness and residual stress of as-built and aged additively manufactured maraging steel post-processed by milling. *Int J Adv Manuf Technol.* <https://doi.org/10.1007/s00170-021-07527-z>

22. Zavala-Arredondo M, London T, Allen M, et al (2019) Use of power factor and specific point energy as design parameters in laser powder-bed-fusion (L-PBF) of AlSi10Mg alloy. *Mater Des.* <https://doi.org/10.1016/j.matdes.2019.108018>
23. Schleifenbaum H, Meiners W, Wissenbach K, Hinke C (2010) Individualized production by means of high power Selective Laser Melting. *CIRP J Manuf Sci Technol* 2:161–169. <https://doi.org/10.1016/j.cirpj.2010.03.005>
24. Bartkowiak K, Ullrich S, Frick T, Schmidt M (2011) New developments of laser processing aluminium alloys via additive manufacturing technique. In: *Physics Procedia*
25. Wang T, Dai S, Liao H, Zhu H (2020) Pores and the formation mechanisms of SLMed AlSi10Mg. *Rapid Prototyp J* 26:1657–1664. <https://doi.org/10.1108/RPJ-02-2020-0036>
26. Parveen S, Rao R. U, K D, Telesang G (2021) Investigation on Correlation between Microstructure and Mechanical Properties of AlSi10Mg Specimens by AM Technology. *SSRN Electron J.* <https://doi.org/10.2139/ssrn.3989415>
27. Dadbakhsh S, Hao L (2014) Effect of layer thickness in selective laser melting on microstructure of Al/5 wt.%Fe₂O₃ powder consolidated parts. *Sci World J.* <https://doi.org/10.1155/2014/106129>
28. Tsao CC, Hocheng H (2005) Computerized tomography and C-Scan for measuring delamination in the drilling of composite materials using various drills. *Int J Mach Tools Manuf.* <https://doi.org/10.1016/j.ijmachtools.2005.01.009>
29. Peralta AD, Enright M, Megahed M, et al (2016) Towards rapid qualification of powder-bed laser additively manufactured parts. *Integr Mater Manuf Innov.* <https://doi.org/10.1186/s40192-016-0052-5>
30. Hastie JC, Kartal ME, Carter LN, et al (2020) Classifying shape of internal pores within AlSi10Mg alloy manufactured by laser powder bed fusion using 3D X-ray micro computed tomography: Influence of processing parameters and heat treatment. *Mater Charact* 163:110225. <https://doi.org/10.1016/j.matchar.2020.110225>
31. Raza A, Fiegl T, Hanif I, et al (2021) Degradation of AlSi10Mg powder during laser based powder bed fusion processing. *Mater Des.* <https://doi.org/10.1016/j.matdes.2020.109358>
32. Cordova L, Campos M, Tinga T (2019) Revealing the Effects of Powder Reuse for Selective Laser Melting by Powder Characterization. *JOM.* <https://doi.org/10.1007/s11837-018-3305-2>
33. Maamoun AH, Elbestawi M, Dosbaeva GK, Veldhuis SC (2018) Thermal post-processing of AlSi10Mg parts produced by Selective Laser Melting using recycled powder. *Addit Manuf.* <https://doi.org/10.1016/j.addma.2018.03.014>
34. Del Re F, Contaldi V, Astarita A, et al (2018) Statistical approach for assessing the effect of powder reuse on the final quality of AlSi10Mg parts produced by laser powder bed fusion additive manufacturing. *Int J Adv Manuf Technol.* <https://doi.org/10.1007/s00170-018-2090-y>
35. Yu W, Sing SL, Chua CK, Tian X (2019) Influence of re-melting on surface roughness and porosity of AlSi10Mg parts fabricated by selective laser melting. *J Alloys Compd.* <https://doi.org/10.1016/j.jallcom.2019.04.017>
36. Yasa E, Deckers J, Kruth JP (2011) The investigation of the influence of laser re-melting on density, surface quality and microstructure of selective laser melting parts. *Rapid Prototyp J.* <https://doi.org/10.1108/13552541111156450>
37. Han Q, Jiao Y (2019) Effect of heat treatment and laser surface remelting on AlSi10Mg alloy fabricated by selective laser melting. *Int J Adv Manuf Technol.* <https://doi.org/10.1007/s00170-018-03272-y>
38. Spierings AB, Schneider M, Eggenberger R (2011) Comparison of density measurement techniques for additive manufactured metallic parts. *Rapid Prototyp J.* <https://doi.org/10.1108/13552541111156504>
39. Lou S, Jiang X, Sun W, et al (2019) Characterisation methods for powder bed fusion processed surface topography. *Precis Eng.*

<https://doi.org/10.1016/j.precisioneng.2018.09.007>

40. Fox JC, Moylan SP, Lane BM (2016) Preliminary study toward surface texture as a process signature in laser powder bed fusion additive manufacturing. In: Proceedings - ASPE/euspen 2016 Summer Topical Meeting: Dimensional Accuracy and Surface Finish in Additive Manufacturing
41. ISO (2019) BSI Standards Publication Metallic materials - Tensile testing BS EN ISO 6892-1:2019
42. Trevisan F, Calignano F, Lorusso M, et al (2017) On the selective laser melting (SLM) of the AlSi10Mg alloy: Process, microstructure, and mechanical properties. *Materials* (Basel).
43. Shifeng W, Shuai L, Qingsong W, et al (2014) Effect of molten pool boundaries on the mechanical properties of selective laser melting parts. *J Mater Process Technol.* <https://doi.org/10.1016/j.jmatprotec.2014.06.002>
44. Pauly S, Wang P, Kühn U, Kosiba K (2018) Experimental determination of cooling rates in selectively laser-melted eutectic Al-33Cu. *Addit Manuf.* <https://doi.org/10.1016/j.addma.2018.05.034>
45. Prashanth KG, Scudino S, Maity T, et al (2017) Is the energy density a reliable parameter for materials synthesis by selective laser melting? *Mater Res Lett.* <https://doi.org/10.1080/21663831.2017.1299808>
46. Scipioni Bertoli U, Wolfer AJ, Matthews MJ, et al (2017) On the limitations of Volumetric Energy Density as a design parameter for Selective Laser Melting. *Mater Des.* <https://doi.org/10.1016/j.matdes.2016.10.037>
47. Liu M, Wei K, Zeng X (2022) High power laser powder bed fusion of AlSi10Mg alloy: Effect of layer thickness on defect, microstructure and mechanical property. *Mater Sci Eng A* 842:143107. <https://doi.org/10.1016/J.MSEA.2022.143107>
48. Aboulkhair NT, Everitt NM, Ashcroft I, Tuck C (2014) Reducing porosity in AlSi10Mg parts processed by selective laser melting. *Addit Manuf* 1:77–86. <https://doi.org/10.1016/j.addma.2014.08.001>
49. Gordon J V., Narra SP, Cunningham RW, et al (2020) Defect structure process maps for laser powder bed fusion additive manufacturing. *Addit Manuf.* <https://doi.org/10.1016/j.addma.2020.101552>
50. Babamiri BB, Indeck J, Demeneghi G, et al (2020) Quantification of porosity and microstructure and their effect on quasi-static and dynamic behavior of additively manufactured Inconel 718. *Addit Manuf.* <https://doi.org/10.1016/j.addma.2020.101380>
51. Yang K V., Rometsch P, Jarvis T, et al (2018) Porosity formation mechanisms and fatigue response in Al-Si-Mg alloys made by selective laser melting. *Mater Sci Eng A.* <https://doi.org/10.1016/j.msea.2017.11.078>
52. Wadell H (1932) Volume, Shape, and Roundness of Rock Particles. *J Geol.* <https://doi.org/10.1086/623964>
53. Calignano F, Giuffrida F, Galati M (2021) Effect of the build orientation on the mechanical performance of polymeric parts produced by multi jet fusion and selective laser sintering. *J Manuf Process.* <https://doi.org/10.1016/j.jmapro.2021.03.018>
54. Qiu C, Panwisawas C, Ward M, et al (2015) On the role of melt flow into the surface structure and porosity development during selective laser melting. *Acta Mater.* <https://doi.org/10.1016/j.actamat.2015.06.004>
55. Murakami Y (2019) Metal fatigue: Effects of small defects and nonmetallic inclusions
56. Simonelli M, Tuck C, Aboulkhair NT, et al (2015) A Study on the Laser Spatter and the Oxidation Reactions During Selective Laser Melting of 316L Stainless Steel, Al-Si10-Mg, and Ti-6Al-4V. *Metall Mater Trans A Phys Metall Mater Sci.* <https://doi.org/10.1007/s11661-015-2882-8>
57. Guo Q, Zhao C, Escano LI, et al (2018) Transient dynamics of powder spattering in laser powder bed fusion additive manufacturing process revealed by in-situ high-speed high-

- energy x-ray imaging. *Acta Mater.* <https://doi.org/10.1016/j.actamat.2018.03.036>
58. Read N, Wang W, Essa K, Attallah MM (2015) Selective laser melting of AlSi10Mg alloy: Process optimisation and mechanical properties development. *Mater Des* 65:417–424. <https://doi.org/10.1016/j.matdes.2014.09.044>
59. Jawade SA, Joshi RS, Desai SB (2020) Comparative study of mechanical properties of additively manufactured aluminum alloy. *Mater Today Proc.* <https://doi.org/10.1016/j.matpr.2020.02.096>
60. Silvestri AT, Astarita A, Hassanin A El, et al (2020) Assessment of the mechanical properties of AlSi10Mg parts produced through selective laser melting under different conditions. *Procedia Manuf* 47:1058–1064. <https://doi.org/10.1016/j.promfg.2020.04.115>
61. Anwar A Bin, Pham QC (2017) Selective laser melting of AlSi10Mg: Effects of scan direction, part placement and inert gas flow velocity on tensile strength. *J Mater Process Technol.* <https://doi.org/10.1016/j.jmatprotec.2016.10.015>
62. Mfusi BJ, Mathe NR, Tshabalala LC, Popoola PAI (2019) The effect of stress relief on the mechanical and fatigue properties of additively manufactured AlSi10Mg parts. *Metals (Basel)*. <https://doi.org/10.3390/met9111216>
63. Lorusso M, Trevisan F, Calignano F, et al (2020) A357 alloy by lpbfd for industry applications. *Materials (Basel)*. <https://doi.org/10.3390/ma13071488>
64. Ding R, Yao J, Du B, et al (2021) Effect of shielding gas volume flow on the consistency of microstructure and tensile properties of 316L manufactured by selective laser melting. *Metals (Basel)*. <https://doi.org/10.3390/met11020205>
65. Nguyen DS, Park HS, Lee CM (2019) Effect of cleaning gas stream on products in selective laser melting. *Mater Manuf Process.* <https://doi.org/10.1080/10426914.2018.1512132>
66. (1990) *Properties and Selection: Nonferrous Alloys and Special-Purpose Materials*
67. Lumley RN (2008) *Technical Data Sheets for Heat-Treated Aluminum High-Pressure Die Castings.* *Die Cast Eng*